Lattice expansion of LSCF-6428 cathodes measured by in situ XRD during SOFC operation

John S. Hardy*, Jared W. Templeton, Dan J. Edwards, Zigui Lu, Jeffry W. Stevenson

Pacific Northwest National Laboratory, 902 Battelle Blvd, Richland, WA 99352, USA

ABSTRACT

A new capability has been developed for analyzing solid oxide fuel cells (SOFCs). This paper describes the initial results of in situ X-ray diffraction (XRD) of the cathode on an operating anode-supported solid oxide fuel cell. It has been demonstrated that XRD measurements of the cathode can be performed simultaneously with electrochemical measurements of cell performance or electrochemical impedance spectroscopy (EIS). While improvements to the technique are still to be made, the XRD pattern of a lanthanum strontium cobalt ferrite (LSCF) cathode with the composition $La_{0.6}Sr_{0.4}Co_{0.2}Fe_{0.8}O_{3-\delta}$ (LSCF-6428) was found to continually but gradually change over the course of more than 60 h of operation in air under typical SOFC operating conditions. It was determined that the most significant change was a gradual increase in the cubic lattice parameters of the LSCF from 3.92502 Å (as determined from the integration of the first 20 h of XRD patterns) to 3.92650 Å (from the integration of the last 20 h). This analysis also revealed that there were several peaks from unidentified minor phases that increased in intensity over this timeframe. After a temporary loss of airflow early in the test, the cell generated between 225 and 250 mW cm^{-2} for the remainder of the test. A large low frequency arc in the impedance spectra suggests the cell performance was gas diffusion limited and that there is room for improvement in air delivery to the cell.

1. Introduction

$La_{0.6}Sr_{0.4}Co_{0.2}Fe_{0.8}O_{3-\delta}$ (LSCF) is an attractive cathode material because it is a mixed ionic and electronic conductor, meaning that sites where oxygen exchange reactions can occur are distributed over the entire surface of the cathode rather than only at the triple phase boundary between the electrolyte, cathode, and gas phases, as is the case for purely electronic conducting cathode materials like lanthanum strontium manganite (LSM). However, one shortcoming of LSCF cathodes is that they are prone to high rates of degradation in performance. There are various mechanisms to which this degradation has been attributed, including chromium poisoning [1–11], strontium segregation [8–16], humidity in the cathode gas [1,12,13], silicon poisoning [13], and gadolinium diffusion from the barrier layer [16]. Besides chromium poisoning, it has been difficult to definitively correlate decreasing performance during operation to these mechanisms or to determine which mechanism is dominant. It is hoped that the herein described research tool can be employed to shed additional light on the source of degradation in LSCF cathodes.

XRD has proven to be a powerful laboratory tool for gaining an increased understanding of SOFC cathode materials. Many XRD studies of these materials have been termed in situ, where in situ means that the XRD patterns were collected at high temperature and/or in a controlled gas atmosphere. Such in situ XRD studies of LSCF have provided valuable information regarding its thermal and chemical expansion coefficients and phase stability [17–21]. The present study demonstrates a recently developed capability for in situ XRD analysis of SOFC cathode materials wherein XRD is performed on the cathode of an operating anode-supported SOFC while cell performance data is simultaneously being collected. This gives rise to the possibility of correlating changes in one or more of the many aspects of the cathode material that can be monitored by XRD, including compositional changes, phase transformations, lattice strains, and crystallite coarsening, to changes in cell performance that occur over time or due to contaminants or to changes in operating parameters such as voltage, temperature, or cathode gas oxygen content. Outside of electrochemical methods, only a few other analytical techniques have been developed that are capable of monitoring a component of an SOFC with a typical full cell configuration while it is operating under normal conditions (e.g., an anode-supported cell at 750 °C at constant current approximating 800 mV in flowing air on the cathode side and flowing moist hydrogen on the anode side). For example, infrared thermal imaging has

* Corresponding author. Tel.: +1 509 375 2627; fax: +1 509 375 2186.
  E-mail address: john.hardy@pnnl.gov (J.S. Hardy).

been performed on cathodes [22,23] and anodes [24,25] of operating SOFCs, interferometry has been utilized to measure the surface deformation of SOFC anodes during cell operation [24], and Raman spectroscopy has been employed to monitor molecular interactions at the surfaces of operating SOFC anodes [25,26]. The work reported here adds one more tool to this small but important collection of techniques that can be used for the real time analysis of operating SOFCs.

Strain in the crystal lattice of LSCF-6428 is induced by changes in its chemical composition and has been documented in several dilatometric and XRD studies. Using XRD, Kuhn and Ozkan [17] determined that the room temperature length of the unit cell increases linearly at a rate of 0.012 Å per 0.1 Co that is replaced by Fe in $La_{0.6}Sr_{0.4}Co_yFe_{1-y}O_{3-\delta}$ when y is between 0.1 and 0.3. Hashimoto et al. [20] also used XRD to study the effects of replacing Co with Fe and of oxygen vacancies on lattice expansion. They found that the length of the pseudo-cubic lattice parameter increased linearly over the entire range of y in $La_{0.6}Sr_{0.4}Co_yFe_{1-y}O_{3-\delta}$ at a rate of about 0.006 Å per 0.1 Co replaced by Fe and at a rate of 0.0834 ± 0.0041 Å per oxygen vacancy created in the LSCF-6428 unit cell. Tai et al. [27] used XRD to determine that the pseudocubic lattice parameter expands by about 0.006 Å for every 0.1 Sr replaced by La in $La_{1-x}Sr_xCo_{0.2}Fe_{0.8}O_{3-\delta}$ when x is between 0.1 and 0.6. Mineshige et al. [28] investigated the effect of Sr-deficiency in $La_{0.6}Sr_{0.4-z}Co_{0.2}Fe_{0.8}O_{3-\delta}$ on the rhombohedral lattice parameter using XRD and determined that for every 0.1 Sr removed, it expanded by 0.013 Å. This corresponds to a change in the pseudocubic lattice parameter of about 0.009 Å when the rhombohedral angle is near 60°, which applies for LSCF.

2. Experimental

2.1. Cell preparation

Anode-supported electrolyte substrates were fabricated through a non-aqueous tape-casting and lamination process. Green tapes of the 8% yttria-stabilized zirconia (8YSZ) electrolyte, functional anode layer, and bulk anode layer were laminated together. Then circular pieces were cut from the laminate and sintered at 1385 °C for 2 h in air. After sintering, the substrates were approximately 13 mm in diameter and 1 mm thick including an approximately 8 μm thick dense electrolyte membrane. Samaria-doped ceria (SDC) interlayers were applied to the anode-supported 8YSZ membranes by screen printing an ink that was made from 40 wt% SDC powder [Praxair Specialty Ceramics, Woodinville, WA] with an average particle size of approximately 0.2 μm in V-006 binder [Heraeus, West Conshohocken, PA]. The screen printed SDC interlayers were sintered at 1200 °C for 2 h in air. LSCF cathode powder with the nominal composition $La_{0.6}Sr_{0.4}Co_{0.2}Fe_{0.8}O_{3-\delta}$ [Praxair Specialty Ceramics] that had been attrition milled for 5–10 h until the average particle size was approximately 0.35 μm was mixed into V-006 binder at a solids loading of 40 wt%. The resulting ink was applied to the SDC interlayer by screen printing and subsequently sintered at 1100 °C for 2 h. After sintering, the circular cathode had an area of 0.5 cm²; this was considered to be the active cell area when calculating power densities. In order to avoid shielding the cathode from impinging X-rays, gold paste was applied only to the perimeter of the cathode and contacted by a ring of gold mesh for current collection. This left the center of the cathode uncovered. Ni mesh embedded in NiO paste was used as the anode current collector. The cells were sealed with Ceramabond 569 and 685 [Aremco, Valley Cottage, NY] to an alumina test fixture that was developed to allow small-scale button cells to be operated in a high temperature X-ray diffractometer (HTXRD)

while diffraction spectra are being collected from the working cathode.

2.2. Electrochemical cell testing

The test fixture was inserted into the HTK 1200 heating chamber [Anton Paar, Ashland, VA] of the D8 Advance XRD [Bruker AXS, Madison, WI]. The cell was heated to 830 °C for 1 h to sinter the anode current collector and simulate glass sealing of an SOFC stack, and then cooled to the operating temperature of 750 °C. Hydrogen with 3% water vapor was then introduced at a flow rate of 75 sccm to the anode which was allowed to undergo reduction before an operating voltage was applied to the cell. Upon reduction, the composition of the functional anode layer was 50 vol% Ni and 50 vol% 8YSZ and the bulk anode layer was 40 vol% Ni and 60 vol% 8YSZ. Current–voltage and electrochemical impedance spectroscopy (EIS) data were recorded at 750 °C using a Solartron 1480 Multistat and 1255 Frequency Response Analyzer. Performance data was recorded under constant current conditions at the current that was measured when cell operation was initiated at an operating voltage of 800 mV. During intermittent EIS measurements, cells were subjected to a *dc* operating voltage of 0.8 V with a typical *ac* amplitude of 20 mA. Air was supplied to the cathode at 350 sccm.

2.3. X-ray diffraction

10 min scans were repeated continuously from 25 to 85° 2θ with 0.05° steps and a 0.43 s count time per step until cell testing was concluded. The XRD was outfitted with a Cu $K_{\alpha 1}$ radiation source, a Göbel mirror, a 0.12° diffracted beam Soller slit, and a Sol-X energy dispersive X-ray detector [Bruker AXS] that filters out K_β peaks and the fluorescence background due to the presence of Co and Fe.

2.4. Microstructural and chemical analysis

The analysis of the fuel cells in both the untested and tested conditions was performed using a JEOL 7600F field emission gun SEM. This instrument is a high resolution instrument capable of electron probes of 10 nm or less with a maximum of 100 nA. The compositional analysis was performed using an Oxford X-Max 80² silicon drift detector linked to an Oxford INCA computer system. EDS SmartMaps were taken using a high beam current and fine probe to yield a data cube of ~200 million counts at 512 × 384 resolution. Post-processing is performed within the INCA program to yield quantification maps that provide compositional information at each pixel position within the map. The data is then exported to SigmaPlot [v 12.1; Systat Software Inc., Chicago, IL] to generate contour plots.

3. Results and discussion

3.1. Electrochemical performance

The open circuit voltage (OCV) of the anode-supported cell in the XRD test fixture was 1.04 V, which was slightly lower than the 1.07 V OCV we typically obtain with Ceramabond seals but high enough to carry out electrochemical tests. The power density of the cell as a function of time is plotted in Fig. 1. Initially, the cell operated at ~0.33 W cm⁻², however, early in the test, a temporary loss of air flow caused a sharp decline in cell performance that was partially recovered when air flow resumed. Thereafter, the cell generated ~0.25 W cm⁻² with intermittent dips to between 0.23 and 0.24 W cm⁻². While their source was not positively identified, the impedance spectra in Fig. 2 imply that they are associated with an increase in the low frequency polarization arc. Dashed lines are
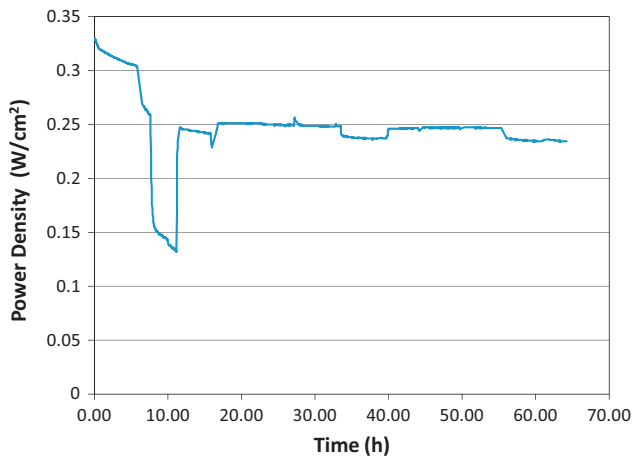
Fig. 1. The power density is plotted as a function of time for an anode supported cell operated in the XRD test fixture.
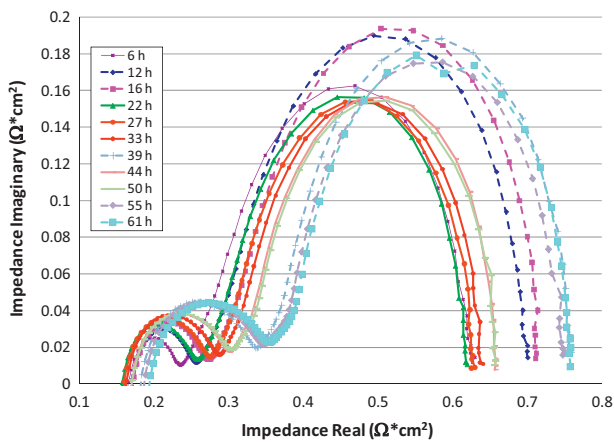

Fig. 2. Electrochemical impedance spectra collected at various times during operation of the cell in the XRD test stand. Dotted lines are used to distinguish the spectra collected during dips in performance.

used in Fig. 2 to discriminate the spectra that were taken during dips in performance. To further illustrate how the impedance spectra change over time and when there are dips in performance, Fig. 3 plots the contributions of ohmic resistance and the high, mid, and
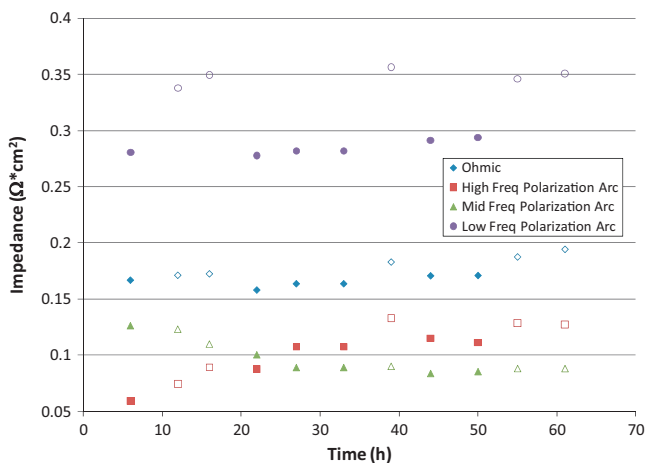

Fig. 3. The results of equivalent circuit modeling of the impedance spectra in Fig. 2. Hollow symbols represent points associated with spectra taken during dips in performance.
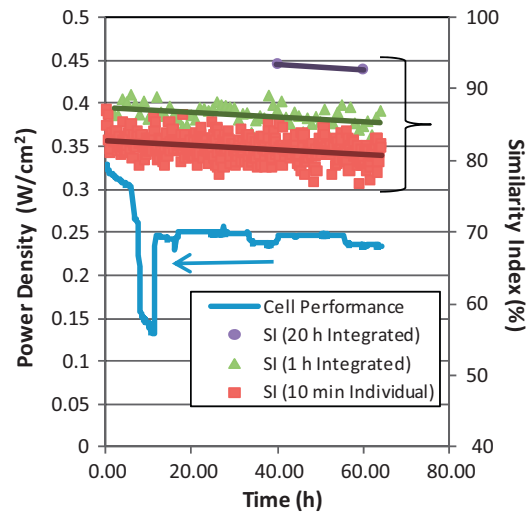

Fig. 4. The similarity index comparing the initial XRD pattern in the series to each successive pattern is plotted together with the cell performance as a function of cell operation time.

low frequency polarization arcs to impedance as a function of time as calculated from equivalent circuit modeling. In this chart, the data collected during dips in performance are discriminated by the use of hollow symbols. Obviously, there are still improvements to be made in achieving smooth, high performance of SOFCs operating in an XRD test fixture while XRD patterns are simultaneously being collected, but as will be pointed out in the next section, the temporary dips in performance did not have an effect on what was occurring on the atomic scale as measured by XRD. Efforts are currently underway to improve air delivery and current collection on the XRD test stand.

3.2. X-ray diffractometry

Jade [v9.3; Materials Data, Inc., Livermore, CA] XRD analysis software has an optional add-on module known as cluster analysis which, when provided a list of XRD patterns, will calculate the similarity index (SI) of each pattern in the list to a seed pattern specified by the user. The similarity index relates how similar the given XRD pattern is to the seed pattern based on a combination of Spearman's
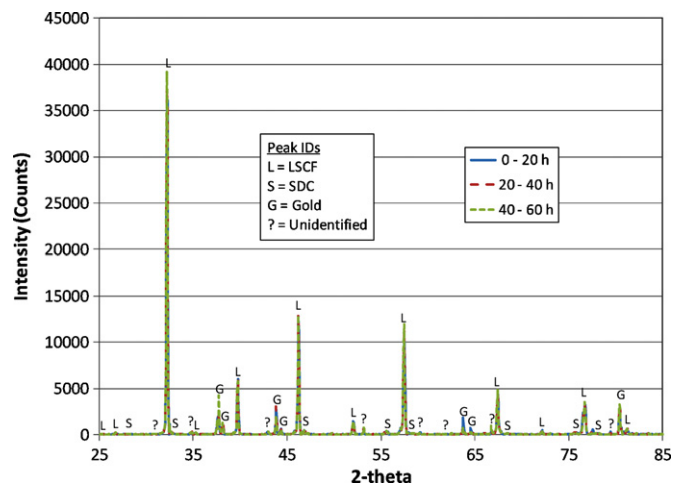

Fig. 5. The individual 10 min XRD scans collected during 20 h intervals of cell operation are integrated together.
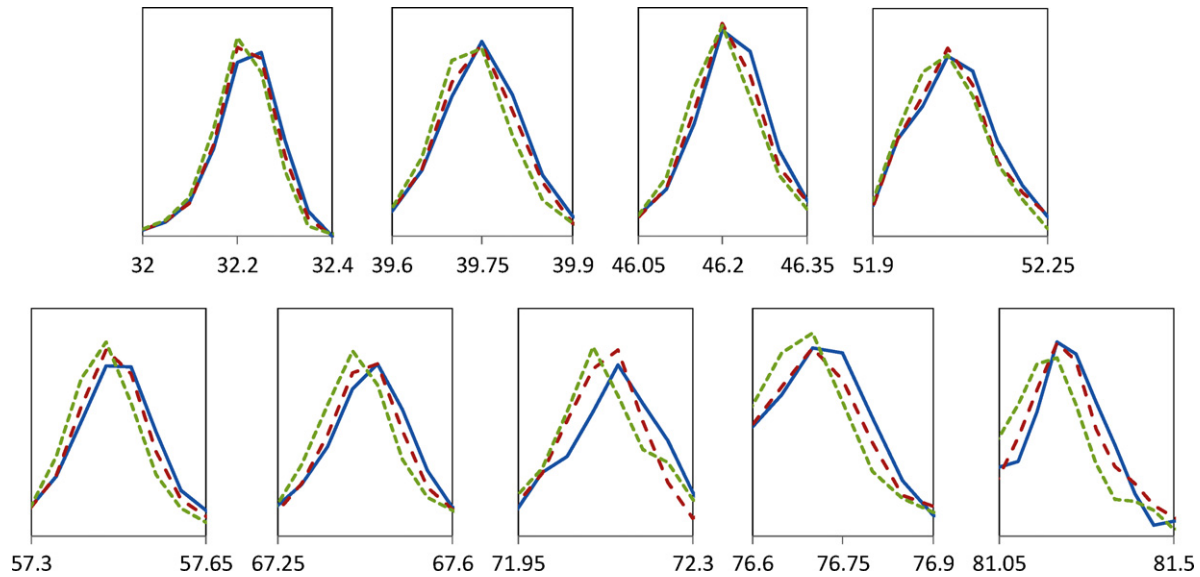
Fig. 6. Nine of the major LSCF peaks from the 20-h integrated XRD patterns. Refer to the legend in Fig. 4.

rank order coefficient (*S*) given in Eq. (1) and Pearson's correlation coefficient (*P*) in Eq. (2).

$$S = \frac{\sum (R(a) \times R(b) - Q)}{\sqrt{\sum \left(R(a)^2 - Q \right) \times \sum \left(R(b)^2 - Q \right)}} \qquad (1)$$

In Eq. (1), $R(x)$ is the rank order of a data point in pattern x and $Q = n(n+1)^2/4$ with n representing the number of data points in the patterns.

$$P = \frac{\sum (I(a) - A) \times (I(b) - B)}{\sqrt{\sum (I(a) - A)^2 \times \sum (I(b) - B)^2}} \qquad (2)$$

In Eq. (2), $I(x)$ is the square root of an intensity in pattern x and X is the average of all $I(x)$ from the pattern.

Similarity indices were calculated using the first pattern in the series as the seed pattern. In Fig. 4, these are plotted as a function of the time at which the final point was collected for the XRD pattern for which the similarity index has been calculated. In order to correlate the XRD data to cell operation, the cell performance data has also been included in Fig. 4. In addition to the data for the individual 10 min XRD scans, similarity indices have also been calculated for XRD patterns integrated over 1 h of cell operation (6 individual scans) and 20 h (120 individual scans) and plotted in Fig. 4. Integrating the scans entails performing a summation of all of the scans collected during the indicated time period, thereby effectively increasing the count times. The point for the first pattern in each series is omitted because it is the seed pattern and therefore the similarity index is 100%. A linear curve fit for each data set indicates that similarity to the initial pattern generally decreases as time progresses meaning that there is a gradual change occurring in the XRD patterns as a function of time. The average rate of change is very similar regardless of whether the individual patterns or integrated patterns are being examined. The similarity index is very sensitive to differences between XRD patterns and the upward shift in the similarity indices for patterns that have been integrated over longer time periods is likely due to the reduction in background noise associated with longer effective X-ray count times which improve the signal to noise ratio. The fact that the dips in cell performance do not have any effect on the magnitude or trend of the similarity index, especially for the 10 min and 1 h patterns, indicates that these small deviations from normal cell performance

did not affect the evolution in the crystal structure that was being reflected in the XRD measurements.

Based upon the findings of the similarity index analysis, the XRD patterns were examined to pinpoint the indicated changes. An overlay of the three 20-h integrated XRD patterns is presented in Fig. 5. LSCF peaks are designated by the letter 'L' and represent the major phase. However, peaks from the SDC interlayer which lies under the cathode were also detected and are marked with the letter 'S'. Peaks from the gold current collector around the perimeter of the cathode are also present and are marked with the letter 'G'. Several minor peaks that could not be identified are labeled '?'. Fig. 6 zooms in on the regions of Fig. 5 in which nine of the major peaks of LSCF reside. In each case, it can be seen that the peak has shifted slightly to lower angles over time as the SOFC operated, indicating an expansion of the crystal lattice. Because the X-rays penetrated through the thickness of the porous cathode, faint peaks from the underlying SDC interlayer were also detected. The regions around eight of these peaks have been expanded in Fig. 7. The peaks from the SDC interlayer provided an internal standard in that none of them displayed the shift to lower angles over time that was observed for the LSCF peaks. This implies that there is no systemic, extrinsic cause for the shifts observed in the LSCF peaks such as a gradual vertical displacement of the cell or some other apparatus-related source of drift in the XRD patterns. This, together with the fact that the integrated XRD patterns represent 20 h of XRD data which translates to effective count times of over 50 s per step and therefore a very high signal-to-noise ratio, and the fact that the similarity indices declined at much the same rate regardless of the time period covered by the XRD patterns, gives a high degree of confidence in the observed lattice expansion of the LSCF cathode material during cell operation.

Furthermore, Fig. 8 focuses on five unidentified peaks in Fig. 5 which appear to be increasing in intensity over the course of cell operation, suggesting that one or more phases may be forming due to reaction, decomposition, or phase segregation of the materials on the cathode side of the SOFC. Several attempts to identify these peaks were unsuccessful. Potential reasons for the difficulty in assigning them include that they are very minor peaks in the pattern implying that the phase giving rise to them is present in very small concentrations. Therefore, a number of the less prominent peaks of the unknown material may not be discernible above the background noise, making it difficult to unambiguously match
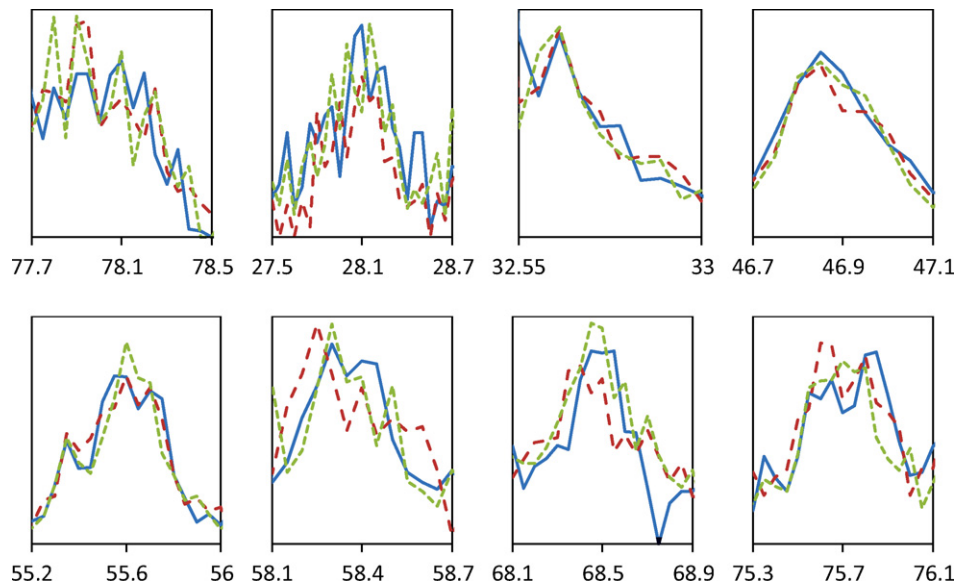
Fig. 7. Eight of the major SDC peaks from the 20-h integrated XRD patterns. Refer to the legend in Fig. 4.
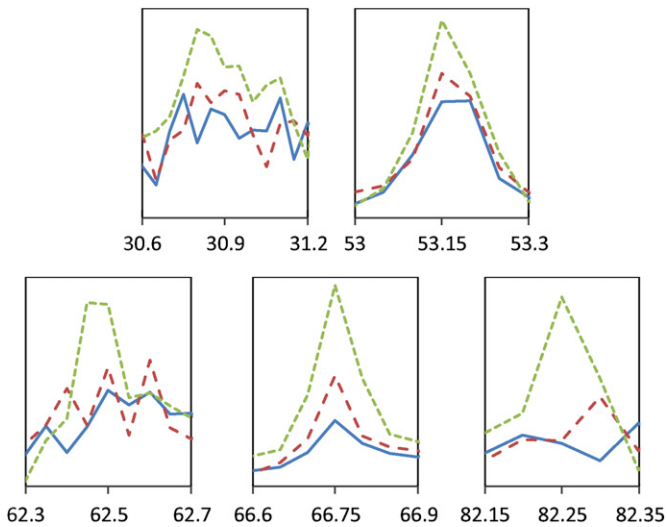

Fig. 8. Five unidentified peaks from the 20-h integrated XRD patterns. Refer to the legend in Fig. 4.

Fig. 9. The cubic lattice parameter of LSCF as calculated from the 20 h integrated XRD patterns using Jade whole pattern fitting and Rietveld refinement.

the peaks to a material in the PDF-4+ 2010 [International Centre for Diffraction Data, Newtown Square, PA] powder diffraction file database. To compound this, the patterns in question were taken at elevated temperature meaning the peaks would have shifted due to thermal expansion from their positions at ambient temperature where most of the reference patterns are measured. Additionally, they may have undergone thermodynamic phase transformations. There is also the consideration that not every material in existence
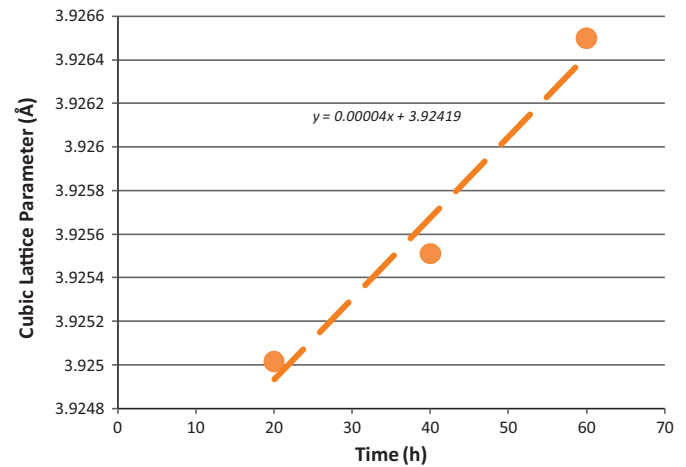
has been included in the PDF. Hence, every year the release of the PDF includes many new entries. The incomprehensive nature of the PDF is especially true in the case of obscure reaction products.

Using Jade software's Whole Pattern Fitting and Rietveld refinement capability, the cubic lattice parameter of the LSCF was calculated from each of the 20-h integrated XRD patterns and plotted in Fig. 9. It should be noted that each point in the chart represents data from a summation of all of the XRD scans collected over the preceding 20 h of operation, as if a series of three 20 h XRD scans had been performed. Thus, it has been plotted such that the point

Table 1
The rate of Sr or Co loss from LSCF-6428 that could account for the rate of lattice expansion measured by XRD is calculated from published composition-induced lattice strain data.

| Reference	Composition-induced	
	Lattice parameter expansion	Calculated rate of segregation during XRD
Tai et al. [27]	~0.06 Å per x in $La_{1-x}Sr_xCo_{0.2}Fe_{0.8}O_{3-\delta}$	~0.0007 Sr from chemical formula per hour
Mineshige et al. [28]	~0.09 Å per z in $La_{0.6}Sr_{0.4-z}Co_{0.2}Fe_{0.8}O_{3-\delta}$	~0.0004 Sr from chemical formula per hour
Hashimoto et al. [20]	~0.06 Å per y in $La_{0.6}Sr_{0.4}Co_yFe_{1-y}O_{3-\delta}$	~0.0007 Co from chemical formula per hour
Kuhn and Ozkan [17]	~0.12 Å per y in $La_{0.6}Sr_{0.4}Co_yFe_{1-y}O_{3-\delta}$	~0.0003 Co from chemical formula per hour
Hashimoto et al. [20]	~0.08 Å per δ in $La_{0.6}Sr_{0.4}Co_{0.2}Fe_{0.8}O_{3-\delta}$	~0.0005 O from chemical formula per hour
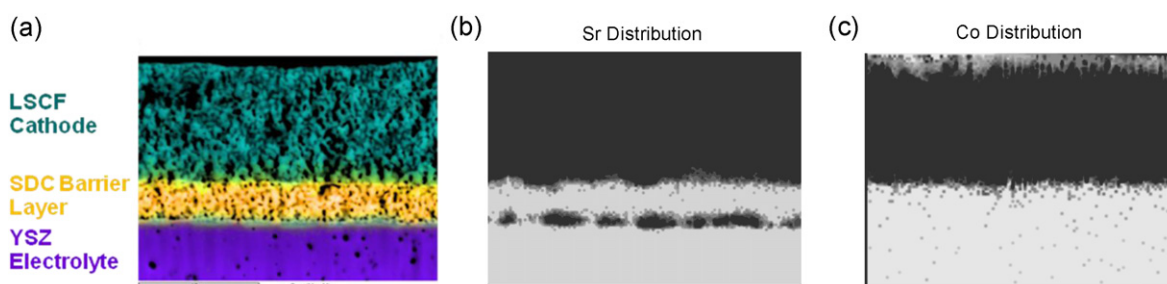
Fig. 10. Field emission SEM of an untested duplicate of the cell tested in the XRD test stand (a) with EDS mapping of Sr (b) and Co (c) distributions designated by dark contrast.
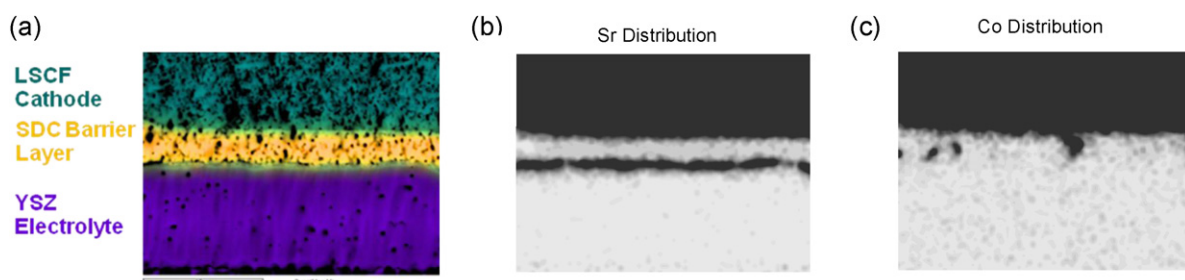

Fig. 11. Field emission SEM of the cell tested in the XRD test stand (a) with EDS mapping of Sr (b) and Co (c) distributions designated by dark contrast.

at 20 h actually represents the entire period from 0 to 20 h of operation. The slope of the best fit line revealed that the lattice parameter expanded at an average rate of approximately 4×10^{-5} Å per hour during 60 h of cell operation. Table 1 summarizes the published reports referenced above of the effects of compositional changes in LSCF on its room temperature pseudocubic lattice parameter and calculates the rates of elemental segregation from the LSCF lattice that might account for the expansion observed in this study. This analysis suggested that a loss of either 0.0004–0.0007 Sr, 0.0003–0.0007 Co, or around 0.0005 O per hour from the chemical formula of LSCF-6428 could account for the average rate of lattice expansion measured by in situ XRD. Because data collected at the SOFC operating temperature of 750 °C is being compared to literature reports that only exist for room temperature, it is believed that some adjustment in the rates of elemental segregation stated above is probably in order, except in the case of oxygen for which measurements were made as a function of temperature and found to be essentially temperature-independent. With regard to the other elements, at the very least it is expected that there would probably be a correction proportional to the amount of thermal and chemical expansion that takes place between room temperature and 750 °C. This expansion is on the order of 1% and would therefore not impact the segregation rates at the level of precision to which they are reported above.

3.3. Microstructural and chemical analysis

Fig. 10a is the SEM image of an untested duplicate of the cell that underwent in situ XRD testing. The image has been colored based on results of elemental mapping by EDS. This clearly delineates the three layers shown as the LSCF cathode, the SDC barrier layer, and the YSZ electrolyte. Fig. 10b and c are elemental maps showing the locations of Sr and Co, respectively, in the cell before electrochemical testing with dark contrast in these areas. Fig. 11 shows the same information for the cell that underwent in situ XRD testing. Comparison of the two sets of images finds that additional Sr has migrated out of the LSCF cathode to the SDC/YSZ interface during electrochemical testing adding to what was already present due to sintering before cell operation, creating a more continuous Sr-rich

layer at this interface. Additionally, large areas of concentrated Co are present in the SDC barrier layer only after operation indicating diffusion of Co out of the cathode during cell operation. There is also an increase in the presence of dilute Co in the YSZ layer after testing. Elemental maps for oxygen are not shown because they were found to be more ambiguous due to the inherent presence of oxygen in each of the components.

4. Conclusions

It was demonstrated that XRD can be performed on the cathode side of an anode-supported SOFC during cell operation and testing. While there is still room for improvement in cell performance in the XRD test fixture, these initial results found that the cubic lattice parameter of the LSCF-6428 cathode material increased at a rate of around 0.00004 Å per hour during cell operation under typical conditions of 750 °C and constant current approximating a 800 mV operating voltage. Published effects of compositional changes in LSCF on the crystal lattice indicate that losses of up to 0.0007 of either Sr or Co per hour from the chemical formula could account for the observed expansion. SEM–EDS analysis comparing the tested cell to a duplicate untested cell supported these possibilities. Elemental mapping of Sr and Co found evidence of increased amounts of both elements having migrated out of the LSCF cathode and into the SDC barrier layer during cell operation.

References

[1] J.J. Bentzen, J.V.T. Hogh, R. Barfod, A. Hagen, Fuel Cells 9 (2009) 823–832.
[2] M.C. Tucker, H. Kurokawa, C.P. Jacobson, L.C. De Jonghe, S.J. Visco, Journal of Power Sources 160 (2006) 130–138.

[3] S.P. Simner, M.D. Anderson, G.G. Xia, Z. Yang, L.R. Pederson, J.W. Stevenson, Journal of the Electrochemical Society 152 (2005) A740–A745.
[4] E. Konysheva, H. Penkalla, E. Wessel, J. Mertens, U. Seeling, L. Singheiser, K. Hilpert, Journal of the Electrochemical Society 153 (2006) A765–A773.
[5] J.W. Fergus, International Journal of Hydrogen Energy 32 (2007) 3664–3671.
[6] J. Guan, S. Zecevic, Y. Liu, P. Lam, R. Klug, M. Alinger, S. Taylor, B. Ramamurthi, R. Sarrafi-Nour, S. Renou, in: K. Eguchi, S.C. Singhai, H. Yokokawa, H. Mizusaki (Eds.), Solid Oxide Fuel Cells, vol. 10, 2007, pp. 405–412.
[7] J.Y. Kim, V.L. Sprenkle, N.L. Canfield, K.D. Meinhardt, L.A. Chick, Journal of the Electrochemical Society 153 (2006) A880–A886.
[8] M.R. Ardigo, A. Perron, L. Combemale, O. Heintz, G. Caboche, S. Chevalier, Journal of Power Sources 196 (2011) 2037–2045.
[9] X.B. Chen, L. Zhang, S.P. Jiang, Journal of the Electrochemical Society 155 (2008) B1093–B1101.
[10] C.W. Sun, R. Hui, J. Roller, Journal of Solid State Electrochemistry 14 (2010) 1125–1144.
[11] H. Yokokawa, H.Y. Tu, B. Iwanschitz, A. Mai, Journal of Power Sources 182 (2008) 400–412.
[12] R.R. Liu, S.H. Kim, S. Taniguchi, T. Oshima, Y. Shiratori, K. Ito, K. Sasaki, Journal of Power Sources 196 (2011) 7090–7096.
[13] E. Bucher, W. Sitte, Solid State Ionics 192 (2011) 480–482.
[14] C. Endler, A. Leonide, A. Weber, F. Tietz, E. Ivers-Tiffee, Journal of the Electrochemical Society 157 (2010) B292–B298.
[15] S.P. Simner, M.D. Anderson, M.H. Engelhard, J.W. Stevenson, Electrochemical and Solid State Letters 9 (2006) A478–A481.
[16] S. Uhlenbruck, T. Moskalewicz, N. Jordan, H.J. Penkalla, H.P. Buchkremer, Solid State Ionics 180 (2009) 418–423.
[17] J.N. Kuhn, U.S. Ozkan, Catalysis Letters 121 (2008) 179–188.
[18] J.N. Kuhn, P.H. Matter, J.M.M. Millet, R.B. Watson, U.S. Ozkan, Journal of Physical Chemistry C 112 (2008) 12468–12476.
[19] N.L.N. Lakshminarayanan, H. Choi, J.N. Kuhn, U.S. Ozkan, Applied Catalysis B: Environmental 103 (2011) 318–325.
[20] S. Hashimoto, Y. Fukuda, M. Kuhn, K. Sato, K. Yashiro, J. Mizusaki, Solid State Ionics 186 (2011) 37–43.
[21] S.J. Xu, W.J. Thomson, Industrial & Engineering Chemistry Research 37 (1998) 1290–1299.
[22] D.J.L. Brett, P. Aguiar, R. Clague, A.J. Marquis, S. Schottl, R. Simpson, N.P. Brandon, Journal of Power Sources 166 (2007) 112–119.
[23] G. Ju, K. Reifsnider, X.Y. Huang, Journal of Fuel Cell and Science and Technology 5 (2008).
[24] H. Guo, G. Iqbal, B.S. Kang, International Journal of Applied Ceramics Technology 7 (2010) 55–62.
[25] B.C. Eigenbrodt, M.B. Pomfret, D.A. Steinhurst, J.C. Owrutsky, R.A. Walker, Journal of Physical Chemistry C 115 (2011) 2895–2903.
[26] E.J. Brightman, R. Maher, D.G. Ivey, G. Offer, N.P. Brandon, ECS Transactions 35 (2011) 1407–1419.
[27] L.W. Tai, M.M. Nasrallah, H.U. Anderson, D.M. Sparlin, S.R. Sehlin, Solid State Ionics 76 (1995) 273–283.
[28] A. Mineshige, J. Izutsu, M. Nakamura, K. Nigaki, J. Abe, M. Kobune, S. Fujii, T. Yazawa, Solid State Ionics 176 (2005) 1145–1149.